Journal of Applied Physics

RESEARCH ARTICLE | FEBRUARY 16 2024

Photothermal defect imaging in hybrid fiber metal laminates using the virtual wave concept FREE

L. Gahleitner ; G. Thummerer ; B. Blank ; J. Wiedemann ; G. Mayr ; C. Hühne ; P. Burgholzer ; U. Cakmak

Check for updates

J. Appl. Phys. 135, 074903 (2024)
https://doi.org/10.1063/5.0188449

View Online
Export Citation
CrossMark

20 February 2024 05:55:31

AIP Publishing

Journal of Applied Physics ARTICLE pubs.aip.org/aip/jap

Photothermal defect imaging in hybrid fiber metal laminates using the virtual wave concept

Cite as: J. Appl. Phys. 135, 074903 (2024); doi: 10.1063/5.0188449
Submitted: 21 November 2023 · Accepted: 28 January 2024 ·
Published Online: 16 February 2024

View Online Export Citation CrossMark

L. Gahleitner,[1,a)] G. Thummerer,[2] B. Blank,[3] J. Wiedemann,[4] G. Mayr,[1] C. Hühne,[4,5] P. Burgholzer,[6] and U. Cakmak[7]

AFFILIATIONS

[1]Research Group of Thermography & NDT, University of Applied Sciences Upper Austria, Stelzhamerstrasse 23, 4600 Wels, Austria
[2]voidsy gmbh, Stelzhamerstrasse 16, 4600 Wels, Austria
[3]Research Group of Computed Tomography, University of Applied Sciences Upper Austria, Stelzhamerstrasse 23, 4600 Wels, Austria
[4]TU Braunschweig, Institute of Mechanics and Adaptronics, Langer Kamp 6, 38106 Braunschweig, Germany
[5]German Aerospace Center (DLR), Institute of Lightweight Systems, Lilienthalplatz 7, 38108 Braunschweig, Germany
[6]Research Center for Non Destructive Testing GmbH, Altenbergerstrasse 69, 4040 Linz, Austria
[7]Johannes Kepler University Linz, Institute of Polymer Product Engineering (IPPE), Altenbergerstrasse 69, 4040 Linz, Austria

[a)]**Author to whom correspondence should be addressed:** lukas.gahleitner@fh-wels.at

20 February 2024 05:55:31

ABSTRACT

This study presents photothermal imaging results of subsurface material defects within fiber metal laminates utilizing the virtual wave concept. Therefore, we theoretically analyze the propagation of the virtual wave signal in a hybrid composite laminate via the method of images. For provoking local material damage, the hybrid composite sample is subjected to a defined impact loading. The results obtained from photothermal defect imaging, utilizing rectangular laser pulse excitation, are compared with results obtained from 3D x-ray computed tomography. To sum up, we demonstrate a fast, non-invasive, and easily interpretable reconstruction of defects within macroscopic hybrid composite laminates based on the virtual wave concept.

Published under an exclusive license by AIP Publishing. https://doi.org/10.1063/5.0188449

I. INTRODUCTION

Fiber metal laminates (FMLs) are a novel kind of the so-called hybrid composite materials, combining suitable properties of both fiber-reinforced polymers and metallic alloys.[1] FMLs are especially used in the aerospace industry as a structural material, for instance, in dominantly unidirectional (UD) loaded structures,[2,3] in components with function integration,[4,5] or in crash structures.[6] Moreover, FMLs are also applied for local material property enhancement, e.g., to increase mechanical bearing strength[7,8] or to enhance erosion resistance.[9,10] In this study, we particularly observe a carbon fiber-reinforced polymer (CFRP) laminate containing thin stainless steel layers.

Due to the special heterogeneous composition of FMLs, numerous subsurface defects can occur during manufacturing or in-service.[11,12] Thus, proper non-destructive testing (NDT) for damage identification and characterization is especially required for this material class. Active infrared thermography (active IRT), a large area and non-invasive NDT technique, has been successfully used for observing damage in composite components in the last few decades.[13,14] Active IRT, in contrast to x-ray computed tomography, does not require ionizing radiation, delivers fast measurement results, and is cost-efficient. Compared to ultrasonic testing, active IRT is particularly suitable for near-surface defect detection of large areas and does not need a coupling medium.

Pulsed thermography (PT), a subcategory of active IRT, enables rapid measurements,[15] especially relevant for inline applications. During the heat diffusion through the sample under test (SUT), which is an irreversible process, entropy production inevitably arises.[16,17] This limits the depth range for defect detection. Thus, raw temperature signals generated from PT must be further post-processed. Various conventional post-processing methods for defect detection are reported in the literature.[18] Thermographic

Published under an exclusive license by AIP Publishing

signal reconstruction (TSR),[19] for instance, fits the measured temperature signal by using polynomial terms. Pulsed phase thermography (PPT),[20] another prominent technique, is based on a transient Fourier transform. Other methods are, e.g., principal component thermography (PCT),[21] which uses a singular value decomposition (SVD) or simple temperature contrast approaches, e.g., differentiated absolute contrast (DAC).[22]

Previous studies report the usage of conventional one-dimensional (1D) evaluation techniques to process data from active IRT for imaging defects in FMLs. Mabrouki *et al.*,[23] e.g., provided a numerical study for modeling PT for FMLs. Montinaro *et al.*[24] studied disbonds in FMLs using laser spot thermography. Prakash *et al.*[25] investigated defects in carbon-flax fiber composites.

In the last few years, interest has developed in applying the so-called reconstruction approaches for PT, in which inverse heat transfer problems (IHTPs),[26] classified as severely ill-posed problems, are solved. By solving IHTPs, the depth or size of defects or internal heat sources, for instance, can be identified. Multidirectional reconstruction approaches account for lateral heat flow. This is especially relevant for accurate defect imaging in highly orthotropic composite parts.[27] Holland and Schiefelbein,[28] for instance, developed a large-scale model-based inversion technique for PT data in the pulse-echo configuration for anisotropic media. Groz *et al.*,[29] e.g., introduced an inversion procedure, based on the fundamental solution of heat conduction, for internal heat sources in anisotropic samples. Another research group[30] used finite difference methods (FDMs) for solving the IHTP for PT signals.

The virtual wave concept (VWC), which has been introduced by Burgholzer *et al.*,[31] is another example for an IHTP. The VWC is, in principle, based on a conversion of a temperature signal into an virtual "acoustic" wave signal. The VWC can account for arbitrary temporal heating patterns and ultrasonic evaluation techniques, such as time-of-flight (TOF), can be used. Moreover, the usage of VWC allows to apply advanced regularization techniques that incorporate a priori information, such as sparsity or positivity.[32] By applying the VWC, inverse heat conduction problems can be solved, which can be modeled using the method of images. The method applies to transient heat conduction problems with boundary conditions of the zeroth, first, and second kind.

In previous work, the VWC has been extended for orthotropic materials by applying ultrasonic reconstruction techniques.[27] Moreover, the computational costs for reconstruction have been significantly reduced.[33] We have applied the VWC for three-dimensional (3D) defect imaging in monolithic CFRP laminates, e.g., for impact damage[34] or for *in situ* delamination growth detection.[35] These observed monolithic structures showed a through-plane homogeneous material behavior in defect-free virtual A-scans.

In our latest research study,[36] we have analyzed the influence of the 1D thermal wave reflection coefficient on the virtual wave propagation in materials with metal substrate. This work discusses the mathematical conversion of temperature signals into virtual wave signals for a body with an internal macroscopic boundary.

To the best of the author's knowledge, this paper demonstrates the application of the VWC for defect imaging in hybrid composite laminates for the first time. The responses in the virtual wave propagation due to the through-plane macroscopic heterogeneous behavior of the FML itself are analyzed and interpreted. This interpretation subsequently allows to distinguish between features associated with the thermal material heterogeneity and defect responses. Furthermore, the measurement results obtained from VWC, using rectangular laser pulse excitation, are compared with results from 3D x-ray computed tomography (3D-XCT) measurements.

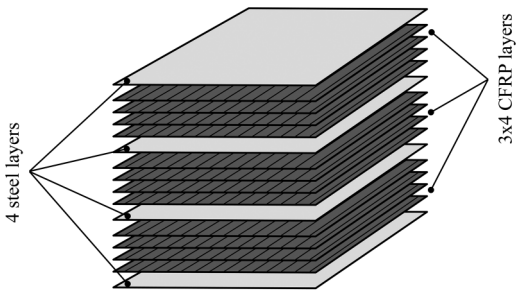

FIG. 1. Principal sketch of the stacking sequence of the observed hybrid laminate, consisting of CFRP prepreg and metallic layers.

This study is organized as follows: In Sec. II, we introduce the observed FML sample and the photothermal reconstruction approach. Section III deals with the interpretation of features from the virtual wave signal for the hybrid composite material. In Sec. IV, we present the used experimental setups. Finally, Sec. V discusses experimental defect imaging results obtained from photothermal testing and from 3D-XCT.

II. MATERIALS AND METHODS

A. Sample preparation

We study a FML sample consisting of CFRP prepreg and stainless steel layers. The stacking sequence is given in Fig. 1. The CFRP material (Hexcel 8552-AS4) has an unidirectional (UD) fiber architecture. Additional layers of stainless steel 1.4310 (X10CrNi18-8) were added according to Fig. 1.

The SUT was cured according to the manufacturer's recommended cure cycle with a final cure step at 180 °C for 120 min in an autoclave process. The cured single CFRP layer thickness is $L_{\text{prepreg}} = 0.13$ mm and the single steel layers have a thickness of $L_{\text{steel}} = 0.12$ mm. The overall sample thickness L_z was approx. 2.00 mm, measured with a micrometer. The corresponding thermo-physical material properties of the FML constituents, e.g., thermal conductivity through plane k_{33}, specific heat capacity c_p and density ρ, are given in Table I. The given thermal conductivity k_{33} denotes the thermal conductivity in the z-direction. After the

TABLE I. Thermo-physical properties of used CFRP[37] and metal material.[38] Note that the given thermal conductivity denotes the thermal conductivity k_{33} through-plane (z-direction according to Fig. 2).

Material	Specification	k_{33}	ρ	c_p
CFRP	Hexcel 8552-AS4	0.61	1580	917
Steel	X10CrNi18-8	15	7900	500

20 February 2024 05:55:31

Published under an exclusive license by AIP Publishing

curing process, the SUT was damaged in the center by an impact with a gas gun with the impact energy of 5 J. The diameter of the impactor was 15.9 mm. The sample dimensions and the considered region of interest (ROI) for photothermal testing are depicted in Fig. 2. The z-axis is the through-plane direction of the SUT.

B. Photothermal reconstruction

The relationship between the temperature signal $T(\mathbf{r}, t)$ from PT and the virtual wave signal $T_{\text{virt}}(\mathbf{r}, t')$ for the same spatial position vector $\mathbf{r}$ is given by a Fredholm integral equation of the first kind according to Burgholzer *et al.*,[31]

$$T(\mathbf{r}, t) = \int_{-\infty}^{\infty} K(t, t')\, T_{\text{virt}}(\mathbf{r}, t')\, \mathrm{d}t' \quad \text{with} \quad K(t, t') = \frac{c}{\sqrt{\pi \alpha t}} \exp\left(-\frac{c^2 t'^2}{4\alpha t}\right) \text{for } t > 0. \tag{1}$$

Herein, α denotes the sample thermal diffusivity through plane, c is the virtual speed of sound through plane, t is the time, and t' denotes an integration variable. In this work, no additional step to account for lateral heat flow for defect sizing was performed. The reconstructed defect size from PT was already in reasonably good agreement with the size obtained from 3D-XCT.

1. Discrete inverse heat transfer problem

Surface temperature signals obtained from PT are discrete in time and space. Thus, Eq. (1) has to be discretized. Consequently, the relationship between the discrete temperature signal $\mathbf{T} \in \mathbb{R}^{N_t \times q}$ and the corresponding discrete virtual wave signal $\mathbf{T}_{\text{virt}} \in \mathbb{R}^{N_{tv} \times q}$ is given as a linear matrix equation for one spatial cross section with pixel number q as[33]

$$\mathbf{T} = \mathbf{K}\mathbf{T}_{\text{virt}}, \tag{2}$$

where $\mathbf{K} \in \mathbb{R}^{N_t \times N_{tv}}$ is the discrete transformation kernel. Herein, N_t is the number of time steps for the temperature signal and N_{tv} is the number of time steps for the virtual wave signal. The component notation of the discrete kernel $\mathbf{K}$ for a Dirac Delta-like heating is finally expressed with $t_k = k\Delta_t$ and $t'_j = j\Delta_{t'}$, using the running variables $k = \{0, 1, 2, \ldots, N_t - 1\}$ and $j = \{0, 1, 2, \ldots, N_{tv} - 1\}$ as[33]

$$K(k, j) = \frac{\tilde{c}}{\sqrt{\pi \Delta_{\text{Fo}} k}} \exp\left(-\frac{\tilde{c}^2 j^2}{4\Delta_{\text{Fo}} k}\right) = \frac{\eta}{\sqrt{\pi k}} \exp\left(-\frac{\eta^2 j^2}{4k}\right), \tag{3}$$

with the dimensionless speed of sound $\tilde{c} = (c\Delta_t)/\Delta_z$, the discrete Fourier number $\Delta_{\text{Fo}} = (\alpha \Delta_t)/\Delta_z^2$, the dimensionless number $\eta = \tilde{c}/(\sqrt{\Delta_{\text{Fo}}})$, the spatial through plane resolution Δ_z, and the temporal resolution $\Delta_t = \Delta_{t'}$. The relationship between the resolution of a virtual wave signal $\Delta_{t'}$ and the spatial resolution through plane is $\Delta_z = c\Delta_{t'}$. The resolution through-plane Δ_z depends on the desired reconstruction accuracy. The resolution in plane $\Delta_x = \Delta_y$ depends on the distance of the IR-camera to the SUT in the setup. For further details, the reader is referred to Thummerer *et al.*[33]

2. Regularization technique

One cannot directly invert the Fredholm Integral Eq. (1) due to the severely ill-posed nature of the inverse heat transfer problem.[39] Thus, it is necessary to apply regularization approaches. In this study, we apply the alternating direction method of multipliers (ADMM) for regularization. The ADMM is an iterative nonlinear reconstruction scheme. The minimization problem for ADMM[32,40] can be denoted as

$$\text{minimize } \frac{1}{2} ||\mathbf{K}\mathbf{T}_{\text{virt}} - \mathbf{T}||_2^2 + \lambda_{\text{ADMM}} ||\mathbf{T}_{\text{virt}}||_1. \tag{4}$$

Sparsity is introduced by an appropriate formulation of the objective function using L_1 norm minimization. Due to the 1-norm $||\mathbf{T}_{\text{virt}}||_1$ in ADMM, the technique allows some steep gradients for the virtual wave signal and it is able to produce a less smooth solution, such as a piece-wise smooth solution. Therefore, we can reduce artificial oscillations in the virtual wave solution. The regularization parameter for ADMM λ_{ADMM} is determined via the L-curve criterion.[32]

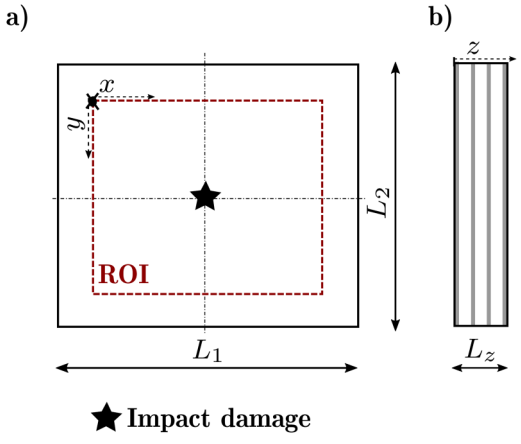

FIG. 2. Geometry of the SUT with (a) top view and (b) side view. The geometrical dimensions are $L_1 = 55$ mm and $L_2 = 55$ mm. The overall sample thickness is $L_z = 2.00$ mm. The impact damage was introduced in the center. The red-dashed rectangle indicates the region of interest (ROI) for active IRT with dimension (26.5×23.7) mm^2.

III. THEORETICAL STUDY

In this section, we theoretically discuss features of the virtual wave propagation for the studied hybrid composite material in a defect-free region, in a first step with Dirac delta pulse heating. This is necessary to clearly distinguish between internal responses from the material itself and subsurface defect features due to the

20 February 2024 05:55:31

Published under an exclusive license by AIP Publishing

damage. Subsequently, the incorporation of finite rectangular laser single-pulse heating is introduced and discussed.

A. Virtual wave propagation in hybrid composite materials for Dirac delta heating

The transient surface temperature difference signal of the considered hybrid material in logarithmic domain at $z = 0$, depicted in Fig. 3(a), was analytically generated with the well established thermal quadrupole method.[41] The thermal quadrupole method allows to construct the temperature signal for a layered material in a convenient way. The inverse Laplace transform was performed with the Euler algorithm.[42] The front surface was excited here by a temporal Dirac-delta pulse with energy $q_{\text{adiab.}} = 3.79 \times 10^3\ \text{J/m}^2$ at time $t = 0$ (initial condition). The considered energy was chosen in order to obtain the same adiabatic temperature plateau as in the real experiment. The front and rear surfaces were assumed to be insulated (adiabatic boundaries).

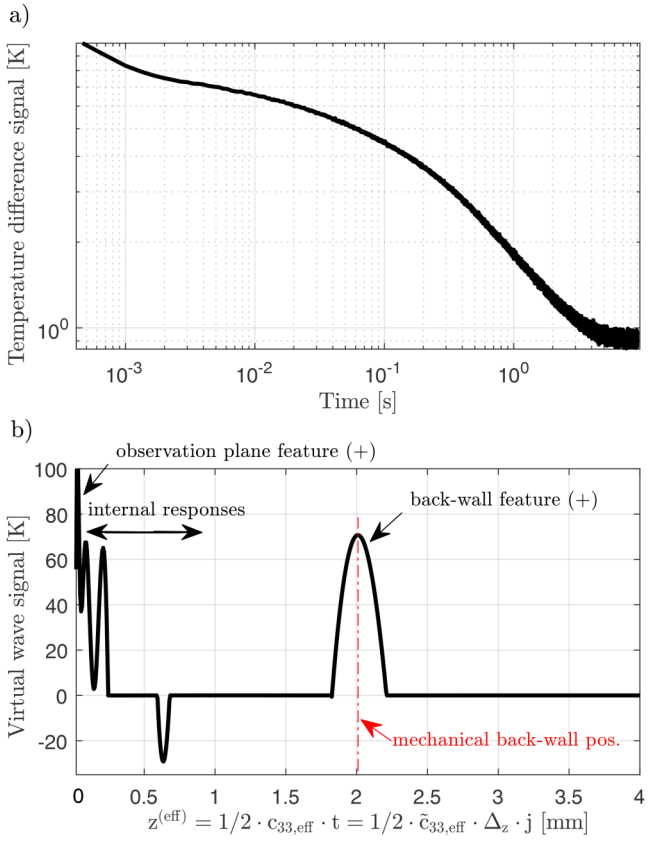

FIG. 3. (a) Temperature signal at $z = 0$ for the studied hybrid material, generated with the thermal quadrupole method and distorted with AWGN. The excitation was a Dirac-delta pulse. The temporal resolution was $\Delta_t = 1/3000$ s. (b) Corresponding virtual wave signal calculated with ADMM, considering effective thermal properties. The spatial resolution through plane was $\Delta_z = 12\,\mu$m. The traveling coordinate was halved in the A-scan due to the double-way heat diffusion. The red-dashed vertical line indicates the mechanical back-wall position of $L_z = 2$ mm.

Additionally, the temperature signal was distorted with additive white Gaussian noise (AWGN) with a standard deviation of $\sigma = 20$ mK for the noise level. The chosen noise level correlates with the real measurement noise in the corresponding photothermal experiment. The usage of AWGN is reasonable, since within a limited temperature range, the variance of the measurement signal from the IR camera can be considered constant,[43] which corresponds to white Gaussian noise. This type of noise is spectrally flat across the entire sampling bandwidth and the amplitude can be modeled with a normal distribution. The temporal resolution was $\Delta_t = 1/3000$ s and the evaluated time was $t_{\text{eval,all}} = 9$ s as in the real experiment. The evaluated time is sufficient to reach the adiabatic temperature plateau.

From the noisy temperature signal of Fig. 3(a), we calculated the corresponding virtual wave signal by evaluating the inverse of the linear matrix Eq. (2). The spatial resolution through-plane was $\Delta_z = 12\,\mu$m, and the number of time steps for the virtual wave signal was $N_{\text{tv}} = 1500$.

First, we use an effective through-plane thermal diffusivity $\alpha_{33,\text{ eff}} = k_{33,\text{ eff}}/(\rho_{\text{eff}}\, c_{\text{p, eff}}) = 3.87 \times 10^{-7}\ \text{m}^2/\text{s}$ for reconstruction. We hereby want to evaluate first, whether we can properly reconstruct the back-wall position by considering effective material properties for reconstruction based on the VWC. Therefore, we use a simple serial model[44] for the through-plane thermal conductivity $k_{33,\text{ eff}}$ and volumetric averaging for the density ρ_{eff} and specific heat capacity $c_{\text{p, eff}}$.

Figure 3(b) depicts the calculated virtual wave signals from ADMM in A-scan representation. In the virtual A-scan, the amplitude of the virtual wave signal is plotted vs the traveling distance for one single pixel. The considered traveling distance $1/2 \cdot c_{33,\text{ eff}} \cdot t$ was halved due to double-way heat diffusion. One can observe an initial source (+) response at $z = 0$ due to the heating of the observation plane. The position of the back-wall source (+) is in good agreement with the real mechanical back-wall position (red-dashed vertical line) of $L_z = 2.00$ mm, when we consider an effective through-plane thermal diffusivity $\alpha_{33,\text{ eff}}$ from a serial model. For the back-wall detection, we can treat the material obviously as thermal homogeneous, since the scale of through-plane heterogeneity is much smaller than the minimum involved thermal wavelength.[45,46]

In addition to previously discussed features, further internal source (+) and sink (−) responses are clearly evident in the defect-free A-scan of Fig. 3(b). Therefore, Fig. 4 depicts a comparison of virtual A-scans from ADMM for the studied hybrid material and for a perfect effective material with thermal diffusivity $\alpha_{33,\text{ eff}}$ and thickness of $L_{\text{eff}} = 2$ mm. The surface temperature signal for the perfect effective material was also generated with the thermal quadrupole method and distorted with AWGN. The perfect effective material does not show internal responses in the A-scan as expected.

Figure 4 clearly indicates a macroscopic heterogeneous thermal through-plane material behavior for small thermal diffusion times for the hybrid material. The responses associated with the heterogeneity are explained in detail below. For small diffusion times, numerous high-frequency components of the thermal wave are still available.[47]

20 February 2024 05:55:31

Published under an exclusive license by AIP Publishing

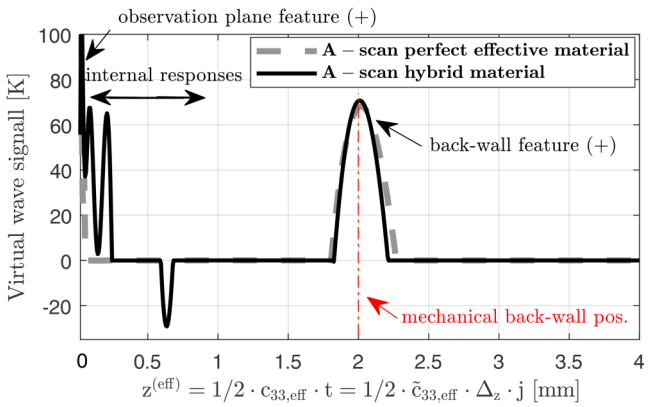

FIG. 4. Virtual wave signals for the studied hybrid material (black) and a perfect effective material with $\alpha_{33,\,\mathrm{eff}} = 3.87 \times 10^{-7}\,\mathrm{m^2/s}$ (dashed). The spatial resolution through plane was $\Delta_z = 12\,\mu\mathrm{m}$. The red-dashed line indicates the real back-wall position of 2 mm.

In the next step, we discuss the solution of the virtual wave signal for a Dirac-delta pulse excitation in the time domain until the second macroscopic material interface is reached. We choose this particular time domain, since in this domain the defect-free A-scan shows additional internal responses due to the macroscopic through-plane heterogeneity. Thus, the evaluation end time $t_{\mathrm{eval,end}} = 0.65\,\mathrm{s}$ was estimated with $L^2_{\mathrm{steel,layer}}/\alpha_{\mathrm{steel}} + L^2_{\mathrm{UD,layer}}/\alpha_{33,\mathrm{UD}}$ using the thickness $L_{\mathrm{steel,layer}} = 0.12\,\mathrm{mm}$ and $L_{\mathrm{UD,layer}} = 4 \cdot L_{\mathrm{prepreg}} = 0.52\,\mathrm{mm}$ and the thermal diffusivity through plane for steel and CFRP, calculated from the parameters in Table I.

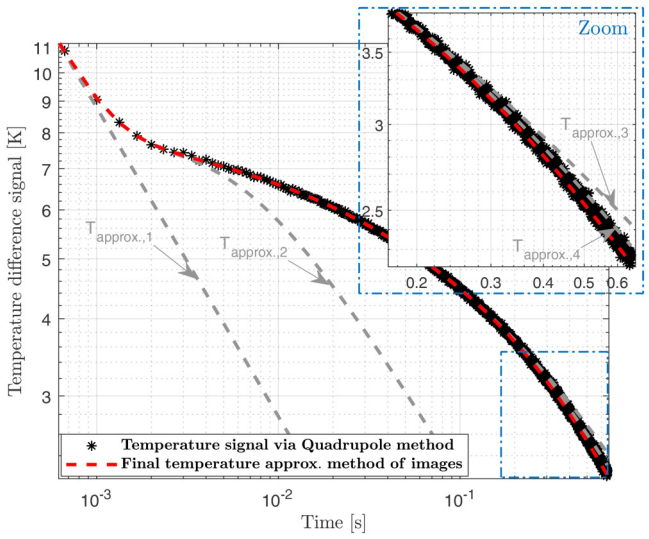

FIG. 5. Surface temperature signal (asterisks) within the evaluation end time $t_{\mathrm{eval,end}} = 0.65\,\mathrm{s}$, which was generated with the thermal quadrupole method. The temporal resolution was $\Delta_t = 1/3000\,\mathrm{s}$. The blue dashed-dotted rectangular indicates the zoomed section. The red-dashed line is the final approximated temperature solution $T_{\mathrm{approx.,\,5}}$ from the method of recursive images[48] according to the Appendix.

The temporal resolution Δ_t was again 1/3000 s. This resulted in a number of time steps for the temperature signal of $N_t = 1938$. In Fig. 5, the respective surface temperature signal, again generated with the thermal quadrupole method and distorted with AWGN, is depicted in logarithmic domain as asterisks.

For a deeper understanding, we describe the noisy temperature signal using the method of images for layered materials proposed by Dias[48] for Dirac delta heating. Generally, the method of recursive images from Dias[48] allows to construct exact solutions, based on the semi-infinite (si) solution of the front layer, due to the incorporation of infinite number of terms. Since the successive temperature responses become rather small, we only consider an approximated solution with a limited number of responses for an easier interpretation. The considered temperature approximation terms in this research are described in detail in the Appendix.

Figure 5 depicts the approximation from the method of recursive images, for the surface temperature solution. We illustrate the successive consideration of approximation terms (see the Appendix) with gray-dashed lines. The final approximation is given as a red-dashed line. One can notice that the temperature signal can already be properly represented with limited terms for all considered time steps. Additional terms would not lead to significant changes of the temperature signal and thus the incorporation of limited terms, especially for describing the noisy signal in this research, is already plausible. The authors want to further emphasize that the residuum temperature between the final approximation (red) and the noisy temperature signal (asterisks) is already within the distortion noise for all considered time steps of Fig. 5.

From the noisy signal (asterisks), given in Fig. 5, we calculated the regularized virtual wave signal. The spatial resolution through-plane was again $\Delta_z = 12\,\mu\mathrm{m}$ and number of time steps for the virtual wave signal was $N_{\mathrm{tv}} = 800$. In Fig. 6 the calculated virtual wave signal from ADMM is shown. Note that the traveling coordinate $z^{(\mathrm{steel})} = 1/2 \cdot c_{33,\,\mathrm{steel}} \cdot t$ is depicted. The traveling coordinate denotes the plotted coordinate direction when considering a specific thermal diffusivity in the virtual A-scan. Since the VWC is a feature extraction method, the source (+) and sink (−) responses in the virtual wave signals are in principle associated with significant deviations from the semi-infinite solution in the underlying noisy temperature signal.[33]

The previously approximated surface temperature solution (red-dashed line), which particularly yields significant temperature responses, can be directly converted into an approximated solution for the theoretical virtual wave propagation.[36] In Fig. 6, the source (+) and sink (−) positions for the approximated theoretical virtual wave propagation are given as dashed vertical lines. One can notice a good correlation between the theoretical positions and the response positions obtained from the regularized virtual wave from the noisy temperature signal. Thus, all significant responses from the temperature solution also lead to responses in the virtual wave signal as expected. Consequently, we have demonstrated that the reconstructed responses are unambiguously related to the thermally heterogeneous material behavior in this time domain.

20 February 2024 05:55:31

Published under an exclusive license by AIP Publishing

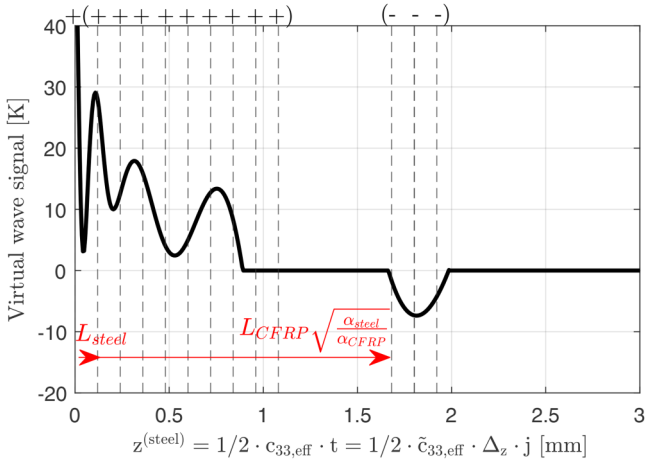

FIG. 6. Corresponding regularized virtual wave signal calculated with ADMM from the noisy temperature signal given in Fig. 5. The spatial resolution through plane was again $\Delta_z = 12\,\mu$m and the traveling coordinate $z^{(steel)}$ was again halved in the A-scan due to the double-way heat diffusion. The dashed vertical lines additionally indicate the positions of the responses from theoretical virtual wave propagation considering finite approximation terms from the method of images. The length L_{CFRP} is defined as $4 \cdot L_{prepreg}$.

From the first mirror source (+) response of Fig. 6 we can, e.g., properly extract the layer thickness of steel of $L_{steel} = 0.12$ mm. Since the thermal wave is highly damped during propagation, the series of source (+) responses in regularized virtual waves cannot be reconstructed as discrete peaks and rather lead to a "smeared" response. However, the regularized virtual wave signal shows a continuous positive amplitude within the region of the theoretical sources (+).

Figure 6 further verifies that we can reconstruct all occurring internal responses from Fig. 3(b) when considering the temperature signal until $t_{eval,end} = 0.65$ s, estimated with $L^2_{steel,layer}/\alpha_{steel} + L^2_{UD,layer}/\alpha_{33,UD}$. This means that we are not able to reconstruct further internal responses when considering larger evaluation times for the considered sample. Thus, it is not necessary to discuss here larger evaluation times for studying the material heterogeneity in the virtual A-scan in principle. We want to emphasize again that for larger evaluation times, the problem already switches to a macroscopic homogeneous material behavior, where the wavelength of the thermal wave is already much larger than the individual boundary layers of the hybrid material.[46,47]

B. Temporal convolution of the transformation kernel for rectangular pulse heating

In the experiment, described in Subsection IV A, we use a thermographic setup with single-pulse laser excitation. The heating pattern is in this case not Dirac delta-like. Thus, we have to account for the finite rectangular heating pulse.

The VWC allows to incorporate any arbitrary heating pattern.[27,49] This is feasible due to the linear nature of the heat and wave equation. Therefore, we have to perform a temporal convolution ($*_t$) of the Dirac delta kernel $\mathbf{K}$ with the considered rectangular laser pulse heating pattern,

$$\mathbf{T} = \mathbf{K}_h \mathbf{T}_{virt} \text{ with } \mathbf{K}_h = \mathbf{K} *_t \mathbf{H}(t). \tag{5}$$

In Fig. 7, the intensity signal for the considered heating pattern $\mathbf{H}(t)$, with pulse length $t_h = 0.17$ s, is depicted. Note that the considered pulse length is identical to the real pulse experiment. The energy of the pulse was $q_{Rect} = 2.213 \times 10^4$ J/m^2 and chosen in order to obtain the same adiabatic temperature as previously from Dirac delta heating. We generate surface temperature signals again with the thermal quadrupole method. Additionally, the signals were distorted with AWGN with an standard deviation of 20 mK.

The generated temperature signals are depicted in Fig. 8(a), again within the evaluation end time $t_{eval,\,end} = 0.67$ s. The pulse excitation length for heating of the observation plane is additionally marked as a vertical dashed line. Figure 8(b) shows the corresponding virtual wave signals, which were obtained with ADMM. For rectangular pulse heating, a temporal convolution ($*_t$) of the Dirac-delta kernel was performed according to Eq. (5). The spatial through-plane resolution for VWC was again $\Delta_z = 12\,\mu$m and the number of time steps for the virtual wave signal was $N_{tv} = 800$. Although the temperature signals from Fig. 8(a) are significantly different, the position of the responses in the virtual wave signals of Fig. 8(b) correlates almost perfectly.

IV. EXPERIMENTAL MEASUREMENTS

A. Setup for photothermal testing

To obtain information about material damage, the SUT was single-pulse laser heated and the surface temperature was observed with an IR-camera. The photothermal setup in the pulse echo configuration (reflection mode) is depicted in Fig. 9. The SUT was insulated at the edges to enable lateral adiabatic boundary conditions. An aluminum tape was adherent to the insulation material, to avoid heating the insulation material itself during the heating pulse.

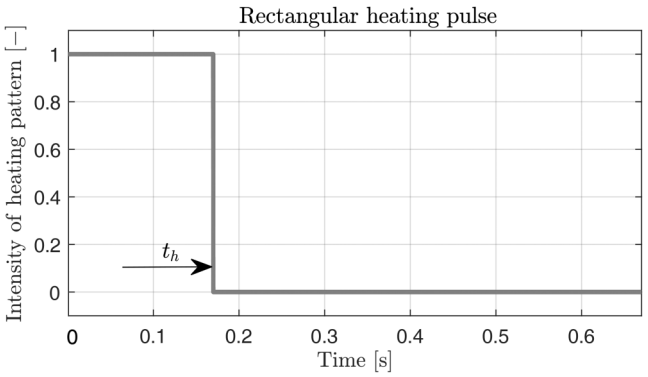

FIG. 7. Intensity profile of considered laser single-pulse heating pattern $\mathbf{H}(t)$. The heating time is $t_h = 0.17$ s.

20 February 2024 05:55:31

Published under an exclusive license by AIP Publishing

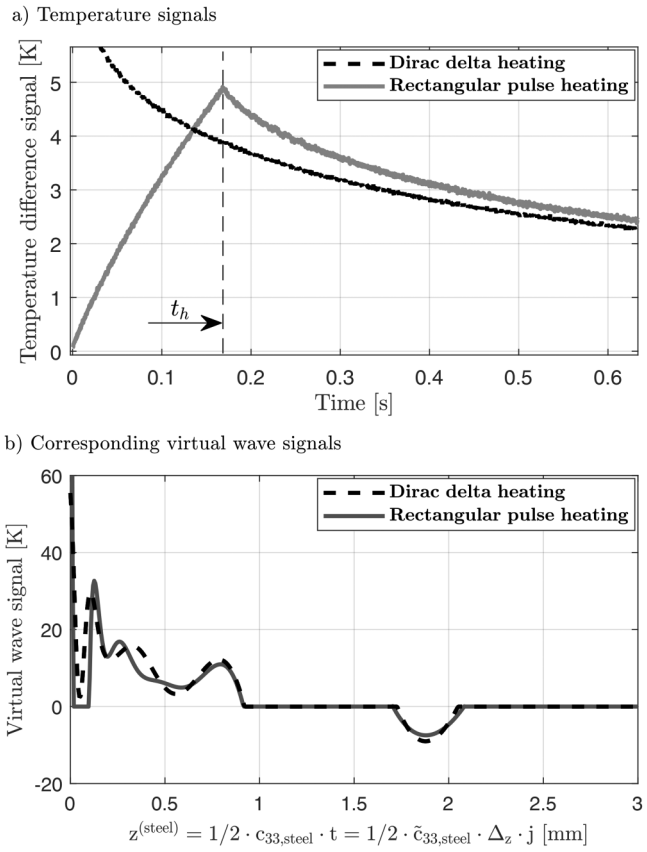

FIG. 8. (a) Surface temperature signal for the hybrid material within the evaluation end time $t_{eval} = 0.65$ s for Dirac delta (black) and rectangular pulse heating (gray). The temperature signals were obtained from the thermal quadrupole method and distorted with an AWGN of 20 mK. The temporal resolution was again $\Delta_t = 1/3000$ s. (b) Corresponding virtual wave signals for Dirac delta heating (black) and rectangular pulse heating (gray). The spatial resolution through plane was $\Delta_z = 12\,\mu$m.

For the measurement of the surface temperature signal, the IR-camera FLIR X6900sc with a temperature resolution (NETD) of smaller than 20 mK was used. The SUT was heated with a diode laser with a power of $P_l = 200$ W for $t_h = 0.17$ s. To enable an uniform excitation of the ROI, a diffractive beam homogenizer (HH-218L-Y-A) was used. The overall measurement time was $t_{meas,\,end} = 9$ s. The temporal resolution was $\Delta_t = 1/3000$ s. The spatial resolution in plane $\Delta_x = \Delta_y$ was approx. 239 μm.

B. Reference measurements with 3D-XCT

Reference measurements of the SUT were performed using 3D x-ray computed tomography (3D-XCT). For this purpose, the Procon CT-Alpha device with a microfokus x-ray tube from X-Ray WorX, which has a maximum tube voltage of 240 kV, was used. The implemented detector, which converts x rays via a scintillation layer into visible light, was a (2048 × 2048) px^2 flat panel detector

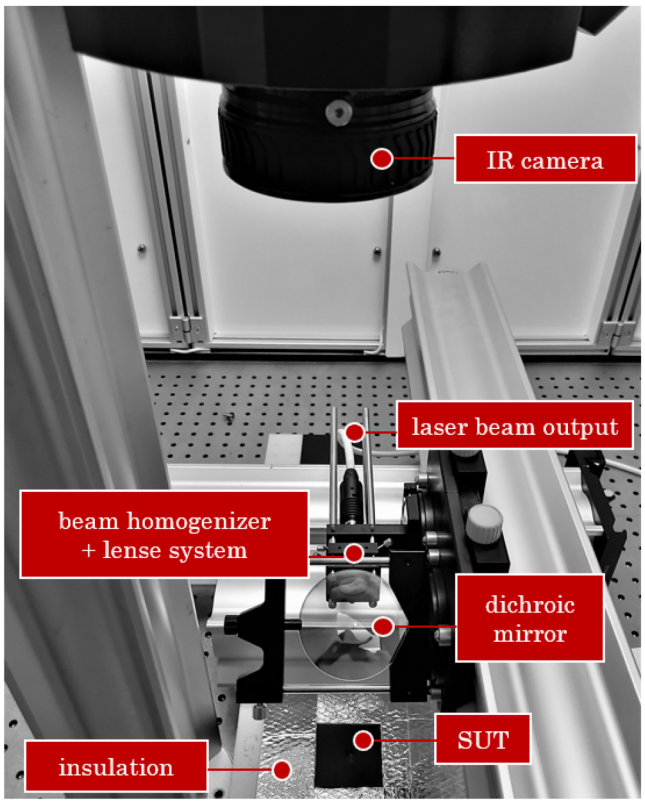

FIG. 9. Photothermal measurement setup in the pulse-echo configuration, consisting of an IR camera, a diode laser for excitation, an optical system, and a sample insulation unit.

from Hamamatsu. The total measurement time for 3D-XCT was approx. 52 min, the number of projections was 1040, the integration time was 3000 ms, the tube voltage was set to 230 kV, and the tube current was 200 μA. The tube was equipped with a tungsten (W) reflection target. The pre-filter used was 1 mm tin (Sn). The 3D-XCT reconstruction including a metal artifact correction was carried out in X-AID software from Mitos GmbH. The voxel size was (40 μm)^3.

V. EXPERIMENTAL RESULTS

In this section, the experimental results from photothermal testing with laser pulse excitation are presented and compared with results obtained from 3D-XCT reference measurements.

A. Virtual wave signals for fiber metal sample

Figure 10(a) exemplary shows a measured surface temperature signal (black line) from single-pulse laser thermography, where the ambient temperature was subtracted, evaluated at the sound pixel position (x,y) = (17,20) px for the overall measurement time $t_{meas,\,end} = 9$ s. From the measured temperature signal, we calculated the corresponding virtual wave signal and incorporated the

20 February 2024 05:55:31

Published under an exclusive license by AIP Publishing

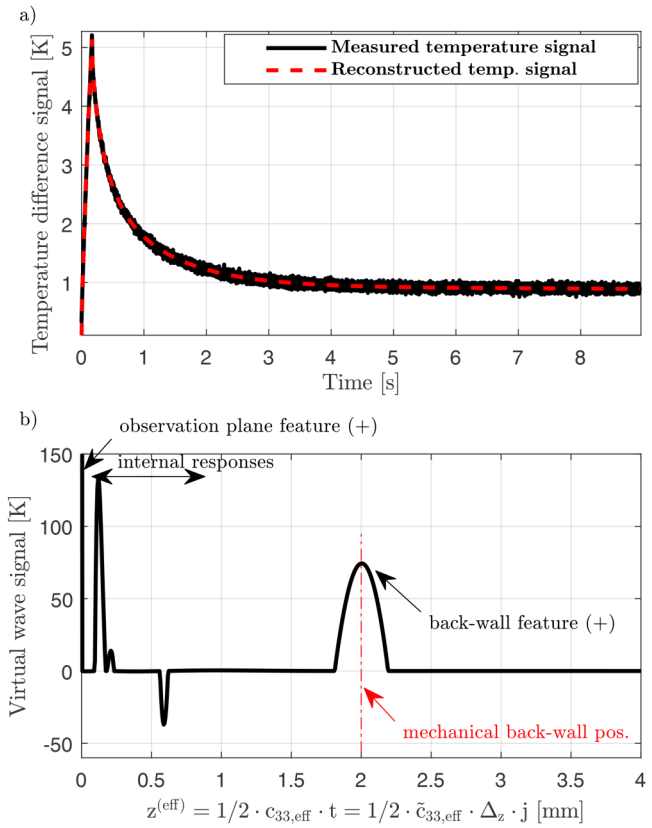

FIG. 10. (a) Measured (black) and reconstructed (red) temperature signal for defect-free position (x,y) = (17,20) px. The temporal resolution was $\Delta_t = 1/3000$ s. (b) Corresponding virtual wave signal calculated with ADMM, considering effective thermal properties. The spatial resolution through plane was $\Delta_z = 12\,\mu$m. The traveling distance was halved in the A-scans due to the double-way heat diffusion. The red-dashed vertical line indicates the mechanical back-wall position.

finite laser pulse heating according to Eq. (5). Figure 10(a) additionally depicts the reconstructed temperature signal $\mathbf{T}_{\text{rec}} = \mathbf{K}_{\text{h}}\mathbf{T}_{\text{virt}}$ (red-dashed line). The reconstructed signal $\mathbf{T}_{\text{rec}}$ is in good agreement with the measured signal $\mathbf{T}_{\text{meas}}$ for all time steps.

Figure 10(b) depicts the corresponding virtual wave signal obtained from ADMM regularization. The spatial resolution through plane was again $\Delta_z = 12\,\mu$m and the number of time steps for the virtual wave signal was $N_{\text{tv}} = 1500$. The effective through-plane thermal diffusivity $\alpha_{33,\,\text{eff}} = k_{33,\,\text{eff}}/(\rho_{\text{eff}} c_{\text{p,\,eff}})$, as introduced in Subsection III A, was first used for VWC reconstruction. The real mechanical back-wall position (vertical line) is found to be in accordance with the reconstructed source (+) response from experimental data generated from laser excitation. Further note that the calculation time for the virtual wave within the whole ROI of $(26.5 \times 23.7)\,\text{mm}^2$ on a standard computer with 16 GB RAM and a processor with 4 cores and 8 threads was only 42 s.

In analogy to Subsection III A, we now study the virtual wave signal until the evaluation end time $t_{\text{eval,end}} = 0.65$ s, which was estimated with $L^2_{\text{steel,layer}}/\alpha_{\text{steel}} + L^2_{\text{UD,layer}}/\alpha_{33,\text{UD}}$. We want to emphasize again that in this time domain, the virtual wave signal shows internal responses due to the through-plane material heterogeneity.

Figure 11(a) gives surface temperature signals for the exemplary defect pixel position (x,y) = (61,57) px, within the delamination region, and for a sound position at (x,y) = (17,20) px. The evaluated defect position is indicated in Fig. 16(a) as red-dashed lines. Figure 11(b) depicts the corresponding virtual wave signals, which were calculated with the ADMM regularization scheme. The traveling coordinate $1/2 \cdot c_{33,\,\text{steel}} \cdot t$ is depicted in the A-scan representation. The number of time steps for the virtual wave signal was $N_{\text{tv}} = 800$. Since we have discussed the features for the defect-free virtual wave propagation in the material in Subsection III A, we can now assign the appearing defect features due to the impact damage in the virtual A-scan.

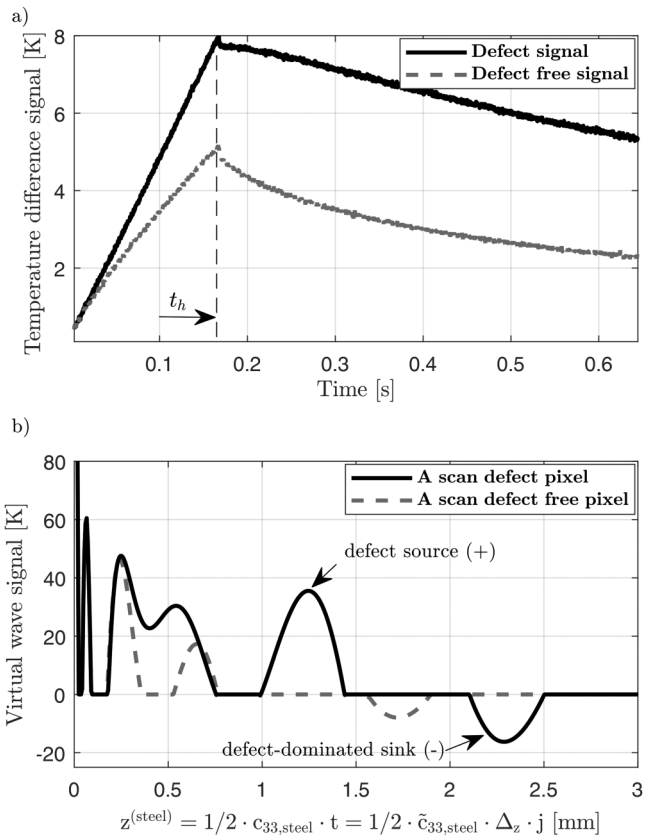

FIG. 11. (a) Exemplary defect (black) temperature signal evaluated at pixel position (x,y) = (61,57) px and defect-free (gray-dashed) temperature signal at position (x,y) = (17,20) px. Both signals were evaluated until $t_{\text{eval,end}} = 0.65$ s. (b) Corresponding virtual wave signals calculated with ADMM, considering the traveling coordinate $z^{(\text{steel})} = 1/2 \cdot c_{33,\,\text{steel}} \cdot t$. The spatial resolution through plane was again $\Delta_z = 12\,\mu$m.

20 February 2024 05:55:31

Published under an exclusive license by AIP Publishing

Figure 11(b) demonstrates that the virtual wave signal for the defective pixel position (black line) differs significantly from the sound position (gray-dashed line). Due to the delamination, heat is trapped above the defect boundary and thus consequently an additional lateral heat flux is initiated.[34] This results here in a defect source (+) and defect-dominated sink (−) in the virtual A-scan. The defect-dominated sink (−) in Fig. 11(b) is a superposition of the sink due to the defect and a sink due to the material composition. All other responses in the sound and defective A-scan, except the observation plane source (+), appear exclusively due to the through-plane heterogeneous material composition.

Figure 12 gives exemplary cross-sectional images of the virtual wave signal $\mathbf{T}_{\text{virt}}$ obtained from ADMM regularization. The depicted B-scans refer to cross sections constructed by a concatenation of pixel-wise evaluated virtual A-scans for specific spatial positions. Note that for the traveling coordinate, the virtual speed of sound for steel $\tilde{c}_{33,\text{steel}}$ was used. In particular, Fig. 12(a) shows the virtual B-scan from reconstruction for the defect position at y = 57 px and Fig. 12(b) shows the virtual B-scan for the sound position y = 20 px. Figure 12 demonstrates that the defective virtual wave cross section is clearly different compared to the sound cross section.

Additionally, Fig. 13 shows exemplary cross-sectional images of the virtual wave signal $\mathbf{T}_{\text{virt}}$ for the defect position at x = 61 px and for the sound position x = 17 px. In the B-scan of Fig. 13(a), the material defect is again visible. One can notice that the extent of the in-plane damage varies when evaluating in this direction. For the sound region, there is no difference when evaluating in or across the grain direction as expected.

B. Comparison of photothermal imaging results with 3D-XCT measurements

Thus, 3D-XCT can be very powerful for detailed 3D inspection of damage due to impact damage in CFRP,[50] we compare defect reconstruction images from VWC with 3D-XCT measurements for the same depth sequence.

Figure 14 shows exemplary sound cross-sectional images within the physical sample depth sequence from 0 to 640 μm. For VWC imaging, we accounted for the specific thermal diffusivities of the evaluated layers to obtain physical depth information. The cross-sectional images from the virtual wave signal as well as the corresponding cross sections from 3D-XCT, depicted in Fig. 14(c), do not indicate any material damage.

Figure 15 depicts the resulting defective cross-sectional images of the virtual wave signal again in the physical depth sequence of 0–640 μm, wherein the delamination appears. The corresponding cross sections from 3D-XCT are given in Fig. 15(c). Both NDT techniques identify a delaminated region due to the defect. The source (+) due to the defect interface is in accordance with the delamination depth, which has been identified from 3D-XCT measurement.

Figure 16(a) exemplary depicts a mean virtual wave image, which was evaluated for the defect depth sequence (70:N_{tv}:75). Note that this evaluated depth sequence is equal to the sample depth sequence of 490–520 μm. Figure 16(b) illustrates the corresponding reconstructed defect image from 3D-XCT, which was

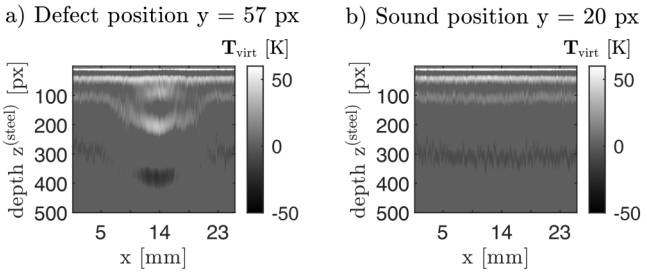

FIG. 12. Cross-sectional images of virtual wave signal $\mathbf{T}_{\text{virt}}$ from ADMM, which were evaluated at (a) the defect position y = 57 px and (b) the defect-free position y = 20 px. Note that the reconstruction was performed with $\tilde{c}_{33,\text{steel}}$. The spatial resolution through plane was $\Delta_z = 12\,\mu$m and the spatial resolution in plane was approx. $\Delta_x = \Delta_y = 239\,\mu$m.

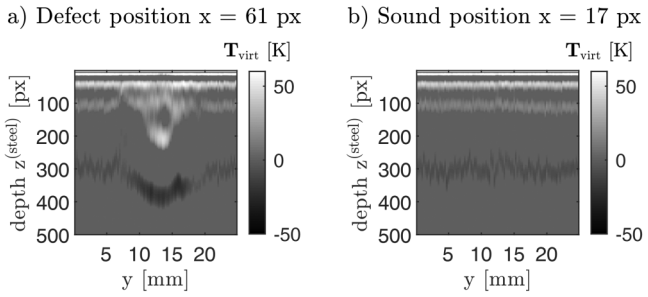

FIG. 13. Cross-sectional images of virtual wave signal $\mathbf{T}_{\text{virt}}$ from ADMM, which were evaluated at (a) the defect position x = 61 px and (b) the defect-free position x = 17 px. Note that the reconstruction was performed with $\tilde{c}_{33,\text{steel}}$. The spatial resolution through plane was $\Delta_z = 12\,\mu$m and the spatial resolution in plane was approx. $\Delta_x = \Delta_y = 239\,\mu$m.

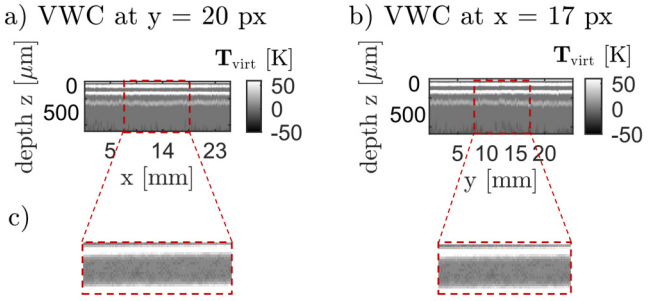

FIG. 14. Sound cross-sectional images of virtual wave signal $\mathbf{T}_{\text{virt}}$ within the physical depth sequence from 0 to 640 μm evaluated at (a) the position y = 20 px and (b) the position x = 17 px. The spatial resolution in plane was approx. $\Delta_x = \Delta_y = 239\,\mu$m. The through-plane resolution was $\Delta_z = 12\,\mu$m. (c) Corresponding 3D-XCT results, which were evaluated for the same depth sequence. The resolution for 3D-XCT measurement was $(40\,\mu\text{m})^3$.

20 February 2024 05:55:31

Published under an exclusive license by AIP Publishing

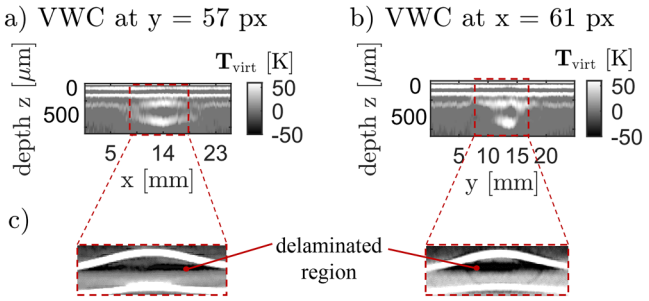

FIG. 15. Defect cross-sectional images of virtual wave signal $\mathbf{T}_{virt}$ within the physical depth sequence from 0 to 640 μm evaluated at (a) the position y = 57 px and (b) the position x = 61 px. The defective POI is depicted in Fig. 16 as red-dashed lines. The spatial resolution in plane was approx. $\Delta_x = \Delta_y = 239\,\mu$m. The through-plane resolution was $\Delta_z = 12\,\mu$m. (c) Corresponding 3D-XCT results, which were evaluated for the same depth sequence. The resolution for 3D-XCT measurement was $(40\,\mu\text{m})^3$.

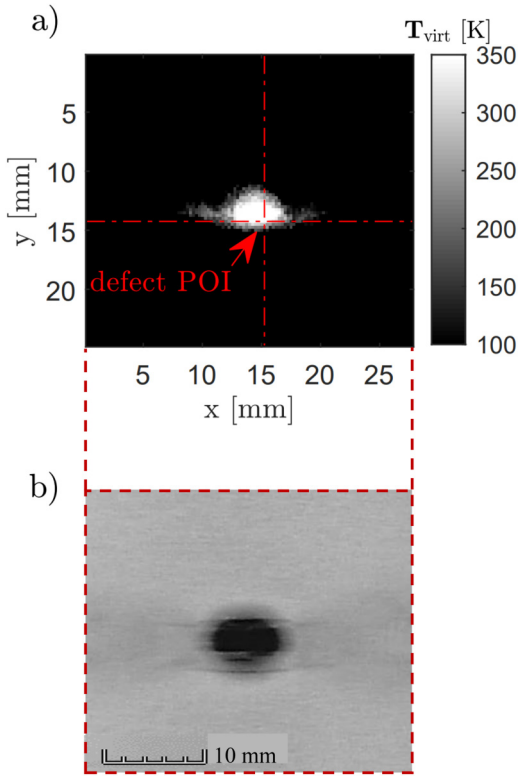

FIG. 16. (a) Mean virtual wave image, which was evaluated within the physical defect depth sequence from 490 to 520 μm. The spatial resolution in plane was approx. $\Delta_x = \Delta_y = 239\,\mu$m. The evaluated defect point of interest (POI) (x,y) = (14.58,13.62) mm, which is equal to (x,y) = (61,57) px, is marked with red dashed-dotted lines. (b) Corresponding mean 3D-XCT defect image, which was evaluated for the same defect depth sequence. The resolution for 3D-XCT measurement was $(40\,\mu\text{m})^3$.

evaluated for the same depth sequence. The reconstructed defect image obtained from photothermal reconstruction is in good accordance with the defect image obtained from 3D-XCT.

VI. SUMMARY AND OUTLOOK

In this study, we applied the virtual wave concept (VWC) for defect imaging in hybrid fiber metal laminates for the first time. We discussed and interpreted the propagation of the virtual wave in a through-plane heterogeneous FML within a defect-free area. We identified internal mirror responses and showed that they are directly related to the heterogeneous material composition. This allowed us to distinguish between features from impact damage and features related to the heterogeneous material composition itself. This is feasible, since the VWC allows to solve all inverse heat conduction problems, which can be formulated with the method of images.

Furthermore, we have performed a temporal convolution of the Dirac delta kernel with the heating function in order to incorporate the finite rectangular laser pulse heating. The experimental results obtained from photothermal reconstruction using the VWC showed good correlation with the results obtained from 3D-XCT.

In the future, it is planned to perform photothermal reconstruction for damaged hybrid laminates, which were previously subjected to different loading scenarios, e.g., bending or torsional loading. We will also apply multi-pulse laser thermography to optimize the available excitation energy for the reconstruction of defects within thick composite components. In addition, future studies will also investigate the application of VWC to reconstruct damage in complex-shaped CFRP components or for structural bondings.

ACKNOWLEDGMENTS

The financial support by the Austrian Research Funding Association (FFG) within the scope of the Production of the Future program within the research project "KombiPhoton" (Contract No. 883919) is gratefully acknowledged. Moreover, financial support is also provided by the FFG within the dissertation funding program of the University of Applied Sciences Upper Austria within the project "Interface" (Contract No. 905121).

AUTHOR DECLARATIONS

Conflict of Interest

The authors have no conflicts to disclose.

Author Contributions

L. Gahleitner: Conceptualization (lead); Data curation (lead); Formal analysis (lead); Investigation (lead); Methodology (lead); Writing – original draft (lead). **G. Thummerer:** Formal analysis (equal); Software (equal); Writing – review & editing (equal). **B. Blank:** Data curation (equal); Validation (lead); Writing – review & editing (equal). **J. Wiedemann:** Resources (equal); Writing – review & editing (equal). **G. Mayr:** Funding acquisition (equal); Project administration (equal); Writing – review & editing (equal). **C. Hühne:** Resources (equal); Writing – review & editing

20 February 2024 05:55:31

Published under an exclusive license by AIP Publishing

(equal). **P. Burgholzer:** Supervision (equal); Writing – review & editing (equal). **U. Cakmak:** Supervision (equal); Writing – review & editing (equal).

DATA AVAILABILITY

The data that support the findings of this study are available from the corresponding author upon reasonable request.

APPENDIX: APPROXIMATION OF TEMPERATURE SIGNAL

The aim of the subsequent steps is to get a deeper inside into the thermal wave propagation within the considered evaluation time $L^2_{\text{steel,layer}}/\alpha_{\text{steel}} + L^2_{\text{UD,layer}}/\alpha_{33,\text{UD}}$ for Dirac delta heating, until the second macroscopic material interface is reached. In this time domain, the virtual wave signal shows internal mirror responses, coming from the material through-plane heterogeneity.

Dias[48] proposed an method for expressing the temperature solution for layered materials via the method of images, which can be constructed from the semi-infinite (si) temperature solution for the first layer. For further details, the reader is referred to Ref. 48. In this study, we only consider a finite number of approximation terms with considerable amplitude values. Note that the five terms $T_{\text{approx, 1}}$, $T_{\text{approx, 2}}$, $T_{\text{approx, 3}}$, $T_{\text{approx, 4}}$, $T_{\text{approx, 5}}$ used for the temperature approximation in Fig. 5 are given in Eqs. (A2)–(A6). It was verified that the incorporation of additional terms does not lead to significant changes in the temperature approximation. The thermal wave reflection and transmission strengths for the studied sample, according to the definition from Dias,[48] are given in Table II. Note that medium I in Table II is denoted as the material in which the thermal wave currently propagates.

The si-temperature solution for the front steel layer incorporating an adiabatic BC and Dirac-delta excitation of the heat introduction plane at $z = 0$ is

$$T_{\text{Z20}}(z, t) = \frac{2\hat{T}_0}{\sqrt{4\pi\alpha_1 t}} \exp\left(-\frac{z^2}{4\alpha_1 t}\right), \tag{A1}$$

with the temperature magnitude $\hat{T}_0 = q_0/(\rho_1 c_{\text{p1}})$, the absorbed heat energy density q_0, the density ρ_1, and the specific heat capacity c_{p1} of the front medium. The energy is absorbed in an infinite thin surface layer $\delta(z)$. Since we are interested in the surface temperature solution, we subsequently evaluate the temperature at the position $z = 0$.

TABLE II. Corresponding thermal wave reflection and transmission strengths for the considered material according to Ref. 48.

Designation	Medium I	Medium II	Value
Refl. strength	Steel	CFRP	$r_1 = 0.78$
Refl. strength	CFRP	Steel	$r_2 = -0.78$
Transm. strength	Steel	CFRP	$t_1 = 1.78$
Transm. strength	CFRP	Steel	$t_2 = 0.22$

When we only consider the above semi-infinite temperature solution of the front medium, we obtain the approximation term,

$$T_{\text{approx, 1}}(0, t) = T_{\text{Z20}}(0, t) = \frac{2\hat{T}_0}{\sqrt{4\pi\alpha_1 t}}. \tag{A2}$$

Second, we additionally incorporate multiple "thermal reflections" (r_1) within the front steel medium to the temperature solution. When we, for instance, only incorporate one successive "thermal reflection" (r_1) and evaluate the solution at the surface position at $z_1 = 0$, we obtain the approximation

$$T_{\text{approx, 2}}(0, t) = T_{\text{approx, 1}}(0, t) + \frac{2\hat{T}_0}{\sqrt{4\pi\alpha_1 t}}\left[2\, r_1 \exp\left(-\frac{(2L_{\text{steel}})^2}{4\alpha_1 t}\right)\right]. \tag{A3}$$

When we incorporate a finite number of successive thermal reflections, since the amplitude of further approximation terms are small, and evaluate the solution again at position $z_1 = 0$, we get the temperature approximation

$$T_{\text{approx, 3}}(0, t) = T_{\text{approx, 1}}(0, t) + \frac{2\hat{T}_0}{\sqrt{4\pi\alpha_1 t}} \cdot \left[2\, r_1 \exp\left(-\frac{(2L_{\text{steel}})^2}{4\alpha_1 t}\right) + 2\, r_1^2 \exp\left(-\frac{(4L_{\text{steel}})^2}{4\alpha_1 t}\right) + \cdots + 2\, r_1^9 \exp\left(-\frac{(18L_{\text{steel}})^2}{4\alpha_1 t}\right) + \underbrace{\cdots}_{\text{neglected}}\right]. \tag{A4}$$

Within the evaluation time, a part of the thermal wave $T_{\text{b,1}}$ is also "transmitted" from the front steel layer to the CFRP layer with transmission strength (t_1). According to Dias,[48] the thermal wave is then whatever "reflected" at the next interface (r_2) or again "transmitted" (t_2). Note that the "transmitted" terms into the second steel layer are neglected for the approximation of the noisy temperature solution for the considered evaluation time. When we now additionally consider a finite number of thermal responses $T_{\text{f,2}}$ from the second medium transmitted back in the front steel layer, we obtain a new approximation of the temperature solution, which was evaluated at the surface position at $z' = L_1$,

$$T_{\text{approx, 4}}(0, t) = T_{\text{approx, 3}}(0, t) + \frac{2\hat{T}_0}{\sqrt{4\pi\alpha_1 t}} \cdot \left[2t_1 r_2 t_2 \exp\left(-\frac{(L_{\text{steel}} + \zeta_1)^2}{4\alpha_1 t}\right) + 2t_1 r_2 t_2 r_1 \exp\left(-\frac{(3L_{\text{steel}} + \zeta_1)^2}{4\alpha_1 t}\right) + \underbrace{\cdots}_{\text{neglected}}\right], \tag{A5}$$

with the term $\zeta_1 = \left(\sqrt{\frac{\alpha_1}{\alpha_2}}\, 2\, L_{\text{CFRP}} + L_{\text{steel}}\right)$.

Finally, we also incorporate multiple "thermal reflections" in the first medium, coming from the responses in the second medium. The approximated temperature solution, evaluated again

20 February 2024 05:55:31

Published under an exclusive license by AIP Publishing

at the surface position $z' = L_1$, according to the method from Dias,[48] is given in Eq. (A6). Note that the "transmitted" thermal waves in this step are not relevant for the studied evaluation time,

$$T_{\text{approx},5}(0,t) = T_{\text{approx},4}(0,t) + \frac{2\hat{T}_0}{\sqrt{4\pi\alpha_1 t}} \cdot \left[2t_1 r_2 t_2 r_1 \exp\left(-\frac{(L_{\text{steel}} + \zeta_2)^2}{4\alpha_1 t} \right) + 2t_1 r_2 t_2 r_1^2 \exp\left(-\frac{(3L_{\text{steel}} + \zeta_2)^2}{4\alpha_1 t} \right) + \underbrace{\dots}_{\text{neglected}} \right], \tag{A6}$$

with the term $\zeta_2 = \left(\sqrt{\frac{\alpha_1}{\alpha_2}} 2\, L_{\text{CFRP}} + 3L_{\text{steel}} \right)$.

In Subsection III A, we have demonstrated that the temperature signal, for the considered time steps, can already be properly described using limited response terms. Note that the temperature signals are visualized in Fig. 5. We also calculated the residuum between the temperature signal generated via the quadrupole method and the final temperature approximation $T_{\text{approx},5}(0,t)$. The residuum was found to be within the distortion noise for all considered time steps. Consequently, this underlines that the incorporation of limited responses, especially for the approximation of noisy temperature signals, is plausible for the presented research. The consideration of additional terms for the description of the noisy surface temperature signal is therefore not necessary.

REFERENCES

[1]A. Asundi and Y. N. C. Alta, "Fiber metal laminates: An advanced material for future aircraft," J. Mater. Process. Technol. **63**, 384–394 (1997).
[2]"Improving impact endangered CFRP structures by metal hybridisation," in *Proceedings of the 12th European Conference on Spacecraft Structures, Materials & Environmental Testing*, edited by D. Stefaniak *et al.* (2012).
[3]D. Stefaniak, "Improving residual strength of unidirectionally reinforced plastic laminates by metal layering," Ph.D. thesis (Technische Universität Carola-Wilhelmina zu Braunschweig, Braunschweig, 2017).
[4]A. Pototzky, D. Stefaniak, and C. Hühne, "Potentials of load carrying conductor tracks in new vehicle structures," in *Technologies for Economical and Functional Lightweight Design*, Zukunftstechnologien für den Multifunktionalen Leichtbau (Springer Vieweg, Berlin, 2019), pp. 79–90.
[5]C. Hühne, C. Ückert, and O. Steffen, "Multifunktionale flügelvorderkante in multimaterialbauweise," Lightweight Des. **9**, 28–33 (2016).
[6]Y. Boose, E. Kappel, D. Stefaniak, R. Prussak, A. Pototzky, and L. Weiß, "Phenomenological investigation on crash characteristics of thin layered CFRP-steel laminates," Int. J. Crashworthiness **27**, 289–298 (2022).
[7]A. Fink, P. P. Camanho, J. M. Andrés, E. Pfeiffer, and A. Obst, "Hybrid CFRP/titanium bolted joints: Performance assessment and application to a spacecraft payload adaptor," Compos. Sci. Technol. **70**, 305–317 (2010).
[8]E. Petersen, D. Stefaniak, and C. Hühne, "Experimental investigation of load carrying mechanisms and failure phenomena in the transition zone of locally metal reinforced joining areas," Compos. Struct. **182**, 79–90 (2017).
[9]D. Düring, L. Weiß, D. Stefaniak, N. Jordan, and C. Hühne, "Low-velocity impact response of composite laminates with steel and elastomer protective layer," Compos. Struct. **134**, 18–26 (2015).
[10]D. Düring, E. Petersen, D. Stefaniak, and C. Hühne, "Damage resistance and low-velocity impact behaviour of hybrid composite laminates with multiple thin steel and elastomer layers," Compos. Struct. **238**, 111851 (2020).
[11]P. Jakubczak and J. Bienias, "Non-destructive damage detection in fibre metal laminates," J. Nondestr. Eval. **38**, 49 (2019).
[12]P. Jakubczak and P. Podolak, "The issue of cai assessment of fibre metal laminates," Compos. Struct. **281**, 114959 (2022).
[13]V. Vavilov and D. Burleigh, *Infrared Thermography and Thermal Nondestructive Testing* (Springer International Publishing, Cham, 2020).
[14]F. Ciampa, P. Mahmoodi, F. Pinto, and M. Meo, "Recent advances in active infrared thermography for non-destructive testing of aerospace components," Sensors **18**, 609 (2018).
[15]V. P. Vavilov and D. D. Burleigh, "Review of pulsed thermal NDT: Physical principles, theory and data processing," NDT&E Int. **73**, 28–52 (2015).
[16]P. Burgholzer and G. Hendorfer, "Limits of spatial resolution for thermography and other non-destructive imaging methods based on diffusion waves," Int. J. Thermophys. **34**, 1617–1632 (2013).
[17]P. Burgholzer, G. Mayr, G. Thummerer, and M. Haltmeier, "Linking information theory and thermodynamics to spatial resolution in photothermal and photoacoustic imaging," J. Appl. Phys. **128**, 171102 (2020).
[18]X. P. V. Maldague, *Nondestructive Evaluation of Materials by Infrared Thermography* (Springer, London, 1993).
[19]S. M. Shepard, "Advances in pulsed thermography," Proc. SPIE **4360**, 511–515 (2001).
[20]X. Maldague and S. Marinetti, "Pulse phase infrared thermography," J. Appl. Phys. **79**, 2694–2698 (1996).
[21]N. Rajic, "Principal component thermography for flaw contrast enhancement and flaw depth characterisation in composite structures," Compos. Struct. **58**, 521–528 (2002).
[22]D. A. González, C. Ibarra-Castanedo, F. J. Madruga, and X. Maldague, "Differentiated absolute phase contrast algorithm for the analysis of pulsed thermographic sequences," Infrared Phys. Technol. **48**, 16–21 (2006).
[23]F. Mabrouki, M. Genest, G. Shi, and A. Fahr, "Numerical modeling for thermographic inspection of fiber metal laminates," NDT&E Int. **42**, 581–588 (2009).
[24]N. Montinaro, D. Cerniglia, and G. Pitarresi, "Detection and characterisation of disbonds on fibre metal laminate hybrid composites by flying laser spot thermography," Composites, Part B **108**, 164–173 (2017).
[25]R. V. Prakash and M. Maharana, "Damage detection using infrared thermography in a carbon-flax fiber hybrid composite," Procedia Struct. Integr. **7**, 283–290 (2017).
[26]M. N. Özisik and H. R. B. Orlande, *Inverse Heat Transfer* (CRC Press, 2021).
[27]G. Thummerer, G. Mayr, and P. Burgholzer, "Photothermal testing of composite materials: Virtual wave concept with prior information for parameter estimation and image reconstruction," J. Appl. Phys. **128**, 125108 (2020).
[28]S. D. Holland and B. Schiefelbein, "Model-based inversion for pulse thermography," Exp. Mech. **59**, 413–426 (2019).
[29]M.-M. Groz, E. Abisset-Chavanne, A. Meziane, A. Sommier, and C. Pradère, "Three-dimensional reconstruction of thermal volumetric sources from surface temperature fields measured by infrared thermography," Appl. Sci. **9**, 5464 (2019).
[30]S. S. Pawar and V. P. Vavilov, "Applying the heat conduction-based 3D normalization and thermal tomography to pulsed infrared thermography for defect characterization in composite materials," Int. J. Heat Mass Transfer **94**, 56–65 (2016).
[31]P. Burgholzer, M. Thor, J. Gruber, and G. Mayr, "Three-dimensional thermographic imaging using a virtual wave concept," J. Appl. Phys. **121**, 105102 (2017).
[32]G. Thummerer, G. Mayr, P. D. Hirsch, M. Ziegler, and P. Burgholzer, "Photothermal image reconstruction in opaque media with virtual wave backpropagation," NDT&E Int. **112**, 102239 (2020).
[33]G. Thummerer, G. Mayr, and P. Burgholzer, "3D photothermal imaging of subsurface defects in composite materials," NDT&E Int. **122**, 102476 (2021).
[34]G. Thummerer, L. Gahleitner, G. Mayr, and P. Burgholzer, "3D photothermal imaging of real subsurface defects in anisotropic media," J. Appl. Phys. **130**, 224901 (2021).
[35]L. Gahleitner, G. Thummerer, B. Reitinger, K. Meirer, and G. Mayr, "3D photothermal reconstruction of subsurface defects in notched multidirectional CFRP laminates due to tensile fatigue loading," NDT&E Int. **131**, 102702 (2022).

20 February 2024 05:55:31

Published under an exclusive license by AIP Publishing

[36]L. Gahleitner, G. Thummerer, G. Mayr, G. Mayr, P. Burgholzer, and U. Cakmak, "One-dimensional photothermal characterization of subsurface interfaces utilizing the virtual wave concept," NDT&E Int. **141**, 102994 (2023).
[37]Hexcel Corporation, "Material data sheet hexcel 8552-as4" (2023); available at https://perma.cc/67TL-T9CC
[38]Deutsche Edelstahlwerke, "Material data sheet 1.4310 steel" (2007); available at https://perma.cc/3A78-55QX
[39]P. C. Hansen, *Discrete Inverse Problems—Insights and Algorithms* (Society for Industrial and Applied Mathematics, 2010).
[40]S. Boyd, "Distributed optimization and statistical learning via the alternating direction method of multipliers," Found. Trends® Mach. Learn. **3**, 1–122 (2010).
[41]J. B. D. Maillet, *Solving the Heat Equation Through Integral Transforms* (Wiley, 2000).
[42]J. Abate and W. Whitt, "A unified framework for numerically inverting laplace transforms," INFORMS J. Comput. **18**, 408–421 (2006).
[43]S. Breitwieser, G. Zauner, and G. Mayr, "Characterization of mid-wavelength quantum infrared cameras using the photon transfer technique," Infrared Phys. Technol. **106**, 103283 (2020).
[44]A. Salazar, A. Sánchez-Lavega, and J. M. Terrón, "Effective thermal diffusivity of layered materials measured by modulated photothermal techniques," J. Appl. Phys. **84**, 3031–3041 (1998).
[45]J. F. Kerrisk, "Thermal diffusivity of heterogeneous materials," J. Appl. Phys. **42**, 267–271 (1971).
[46]J. F. Kerrisk, "Thermal diffusivity of heterogeneous materials. II. Limits of the steady-state approximation," J. Appl. Phys. **43**, 112–117 (1972).
[47]A. Mandelis, *Diffusion-Wave Fields* (Springer, New York, 2001).
[48]C. J. Dias, "A method of recursive images to solve transient heat diffusion in multilayer materials," Int. J. Heat Mass Transfer **85**, 1075–1083 (2015).
[49]H. Plasser, G. Mayr, G. Mayr, G. Hendorfer, and Z. Major, "Enhanced photothermal parameter estimation of thick CFRP in reflection mode for rectangular pulse excitation by halogen lamps," Infrared Phys. Technol. **118**, 103911 (2021).
[50]S. Senck, M. Scheerer, V. Revol, B. Plank, C. Hannesschläger, C. Gusenbauer, and J. Kastner, "Microcrack characterization in loaded CFRP laminates using quantitative two- and three-dimensional x-ray dark-field imaging," Composites, Part A **115**, 206–214 (2018).

20 February 2024 05:55:31

Published under an exclusive license by AIP Publishing